energies

Article

Numerical and Experimental Investigation of a Non-Premixed Double Swirl Combustor

Jiming Lin [1,2,*], Ming Bao [1], Feng Zhang [1], Yong Zhang [1] and Jianhong Yang [1,2]

1 College of Mechanical Engineering and Automation, Huaqiao University, Xiamen 361021, China; 20014080002@stu.hqu.edu.cn (M.B.); zhangfeng@hqu.edu.cn (F.Z.); zhangyonghqu@sina.com (Y.Z.); yjhong1@sina.com (J.Y.)
2 Postdoctoral Workstation, Fujian South Highway Machinery Company, Quanzhou 362021, China
* Correspondence: linjiming@hqu.edu.cn

Abstract: This paper focuses on a detailed numerical investigation combined with experimental research for a non-premixed swirl combustor, which aims to analyze the effects of the blade angle of the outer swirler and equivalence ratio on flow and combustion characteristics. In the experiment, the temperature in the furnace was obtained with a thermocouple, while a realizable *k*-*ε* turbulence model and two-step reaction mechanism of methane and air are used in the numerical method. The calculation results are in good agreement with the experimental data. The results reveal that the air flow rate through the swirler accounts for a small amount of the total air due to the influence of the draft fan, and there is no central recirculation zone (CRZ) despite the presence of the swirler. It was also found that NO emissions gradually decrease as the blade angle of the outer swirler increases. It was also indicated that the average temperature is 100 K higher than the general combustor with a 58° blade angle in the furnace by increasing the equivalent ratio of the tertiary air area, and the NO emissions reduced by approximately 25%. This study can provide guidance for the operation and structural design of non-premixed swirl combustors.

Keywords: non-premixed; swirl combustor; numerical modeling; pollutant emission

check for updates

Citation: Lin, J.; Bao, M.; Zhang, F.; Zhang, Y.; Yang, J. Numerical and Experimental Investigation of a Non-Premixed Double Swirl Combustor. *Energies* **2022**, *15*, 458. https://doi.org/10.3390/en15020458

Academic Editor: F. Xavier Trias

Received: 3 December 2021
Accepted: 8 January 2022
Published: 10 January 2022

1. Introduction

The design of combustion systems can no longer be just about high efficiency and combustion stability, it should continue to be improved in response to the national call for 'Energy Conservation and Emission Reduction' in industry [1]. The combustion system is broadly classified into three categories [2,3]: (1) gas turbines for electricity production and industrial applications, (2) internal combustion engines for transport, and (3) industrial furnaces and burners. The industrial burner for asphalt mixing is used to heat and dry the aggregate. In the meantime, the NO_x emission is a critical factor of air pollution, and achieving low-NO_x generation remains a challenge for different structures and operation schemes.

The swirler plays a significant role in the process of combustion due to its series of advantages, and one of them is to reduce NO_x emissions [4–10]. Many of the 'low NO_x burners' are based on swirl-stabilized flames. These burners achieve low NO_x emissions through the appropriate design of the flame aerodynamics. Boushaki et al. [11] investigated the dynamics of methane-oxygen turbulent non-premixed swirled flames and their emission characteristics with swirl numbers from 0.8 to 1.4, and the consequences indicated that CO_2 could be responsible for NO_x destruction at relatively high oxygen enrichment rates. Zhou et al. [12] studied the effect of primary air pipe on the combustion characteristics of a swirl burner, and the results indicated that, compared with the prototype swirl burner, the NO_x emissions of the optimized burner decreased from 440 to 265 mg/m^3 at 6% O_2. Johnson et al. [13] compared the flow fields and emissions of high-swirl injectors (HSI) and low-swirl injectors (LSI) for gas turbines. They found that NO_x emissions were about 60%

lower than HIS, and the reason may be due to the lack of a strong recirculation zone and the shorter residence time within the LSI. It is well known that the NO_x generation tendency of non-premixed flames is higher than premixed flames [14]. Nevertheless, swirler turned out to be a strong tool for minimizing thermal NO_x by enhancing the mixing efficiency of fuel and air. In addition to the above studies on the flow field characteristics of the single-stage swirler, many scholars began to study the dual-stage swirler to explore its influence on the combustion characteristics of the burner. Almeida et al. [15] studied the influence of global equivalence ratio, Reynolds number, and swirler blade angle of a double-stage swirl burner on flow dynamics and emissions, and the results showed that the NO_x emissions increased when the swirler angle increased. Sung et al. [16] evaluated the effect of swirl vane angle, primary zone stoichiometric ratio, and air staging level on NO_x emissions. They concluded that aerodynamic behaviors had a great effect on NO_x emissions and burnout characteristics by controlling the swirl vane angle. Zeng et al. [17] investigated the combustion characteristics of a counter-rotating, double-stage swirling combustor at constant fuel flow rate. Elbaz et al. [18] investigated the flame stability, NO_x emissions, and flame structure of a burner which had outer and annular swirlers concentric with a central jet. Besides, the burners for optimal design were evaluated in many ways, such as mechanical life, pollution emissions, and combustion stability [19].

Experimental studies enable a quick understanding of combustion phenomena, but due to the complex structure of the burner it is not feasible to test combustion phenomena using experimental methods. Therefore, numerical methods such as computational fluid dynamics (CFD) have come to represent a vital tool. Numerical methods can reduce the design cost and improve the calculation progress, resulting in more research data [20]. Most present calculations rely on Reynolds average Navier–Stokes (RANS), and it is understood that the realizable k-ε RANS model performs reasonably well with swirling flows compared with others, such as the standard k-ε and k-ω SST models [21].

Moreover, Fu et al. [22] studied the generation characteristics of thermal NO_x in a double-swirler combustor, and the results indicated that changes in the number of outer swirls had a greater impact on the generation of thermal NO_x than changes in the number of inner swirls. In this context, it is necessary to investigate the generation of pollutants in depth and take measures to control emissions eventually. At present, though a great deal of research has been done on NO_x generation under the influence of various factors, most of it has focused on swirling. The effect of vortex coupled direct flow on the generation characteristics is rarely considered. So, this work studies the swirler blade angle of the outer swirler and equivalent ratio on NO emissions. If the burner has better combustion characteristics, NO emissions can be reduced.

In this work, a combination of numerical calculations and combustion experiments is used to verify the correctness of the chosen numerical model using experiments, followed by a detailed study through numerical simulations. The focus is on the influence of the blade angle and equivalence ratio of the external swirler on the flow and combustion characteristics. The result is characterised using values such as temperature and emitted NO concentration. These works are used to investigate the combustion characteristics of this burner and the results of these works may guide the design and operation of the non-premixed swirl burner.

2. Experimental Setup and Methodology

As shown in Figure 1, this experimental combustor is made up of four main components, namely the draught fan, fuel pipe, swirler, and furnace. The mainstream air is supplied by a draught fan, and a gas pipe linking to a gas pipeline delivers the fuel (natural gas). The furnace is an arched chamber with a transition cylinder on its inlet. Its length is 11,290 mm. The thermocouples are installed at four test points from T1 to T4 to measure the temperature in the furnace. Four 300 mm-long thermocouples are used to measure the temperature distribution inside the combustor (Platinum/rhodium alloy thermocouple, Type S Product Model Number: WRP-130). The measurement range is 273–1873 K and the measurement accuracy is ±6 K. A cartesian coordinate is established with its origin the center of the combustor exit. As shown in Figure 2a, the swirler includes annular and outer swirlers, and nozzles with different diameters are equally distributed around the inner and outer circumferences of the gas ring. The air flowing through the swirler forms a rotating jet, and the rest of the air forms a straight jet. Figure 2b is a co-rotating swirler used in the present experiments. Table 1 shows the specific structural parameters of a combustor.

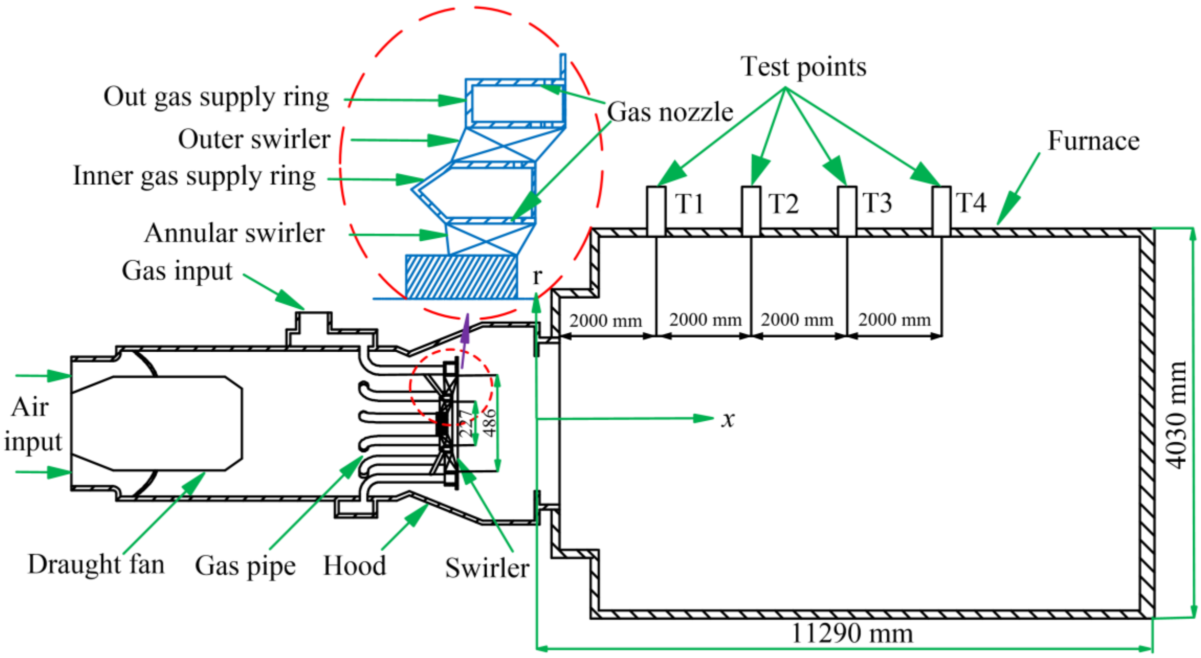

Figure 1. Schematic of the combustor geometry.

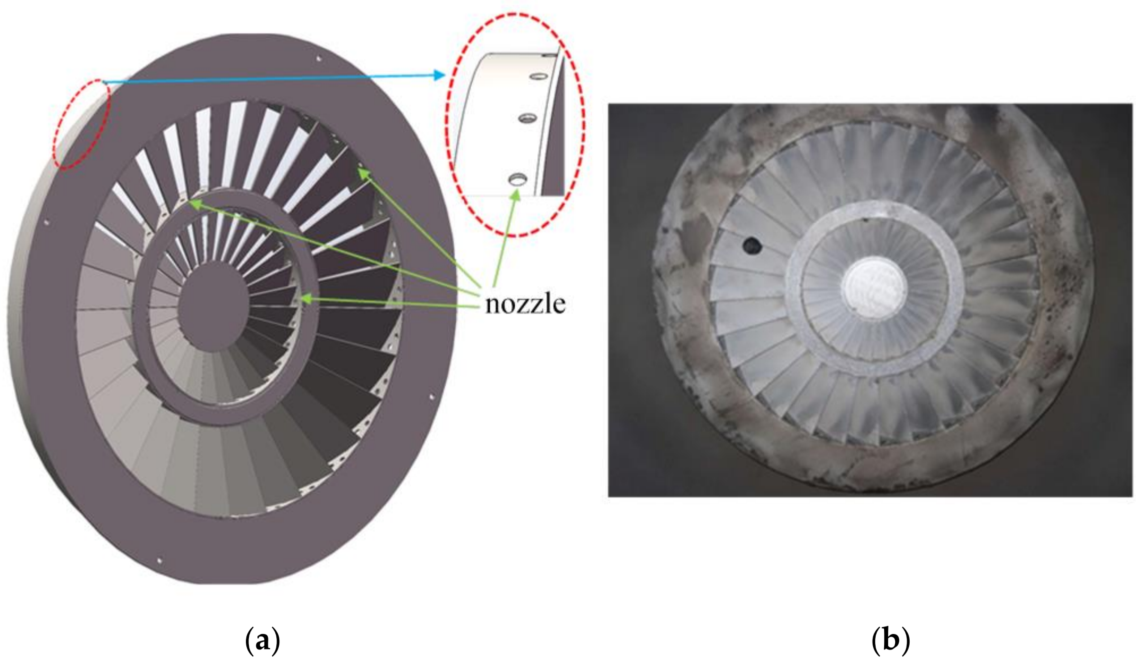

Figure 2. (**a**) Schematic structure of co-rotating swirler; (**b**) the swirler for the experiments.

Table 1. The combustor parameters.

Parameters	Value
Diameter of combustor exit (mm)	830
Inner diameter of inner gas supply ring (mm)	107
Outer diameter of inner gas supply ring (mm)	227
Inner diameter of outer gas supply ring (mm)	280
Outer diameter of outer gas supply ring (mm)	486
Blade number of annular swirler	28
Blade number of outer swirler	28
Install angel of annular swirler (°)	58
Install angel of outer swirler (°)	58
Vane thickness (mm)	1

Swirlers are commonly characterized by the swirl number S, and S is used to reflect the rotating strength. This dimensionless quantity is defined as the ratio between the axial flux of angular momentum G_φ and axial flux of axial momentum G_x, and given by [23]

$$S = \frac{G_\varphi}{G_x R} \tag{1}$$

where R generally takes the jet outlet radius.

The chord length l and the blade angle β are constant for axial swirler, so the axial velocity on the cross-section can be approximately uniformly distributed. Taking $R = R_1$, a simplified expression to calculate S is given by

$$S = \frac{2}{3}\left[\frac{1-(R_0/R_1)^3}{1-(R_0/R_1)^2}\right]\tan\beta \tag{2}$$

where β is the blade angle between the normal direction of the blade and the direction of the airstream. R_0 and R_1 are the inner and outer radius of the blade respectively.

To support later simulation work, the validity and accuracy of the simulation model are verified in this section. The whole facility is engineered for both cold-flow and combustion experiments. Table 2 shows the parameters of the experimental equipment. According to the experimental specification requirements, the frequency of the draft fan is adjusted by the data measured by the Pitot tube to achieve the same boundary conditions of the air inlet. The intelligent swirling vortex flowmeter controls the methane flow rate, and the accuracy is 1% of the measure range. T1–T4 are the thermocouples mentioned in Figure 1. The concentrations of emissions were acquired by means of a flu gas analyzer. Table 3 shows the other parameters used throughout the experiment.

Table 2. Experimental equipment parameters.

Name	Model Number	Range	Accuracy
The Pitot tube	JY-GD680	0–1000 m^3/h	0.5%
The intelligent swirling vortex flowmeter	HP-LUX-DN100YF3E1B1	0–800 m^3/h	1%
Platinum/rhodium alloy thermocouple	Type S, WRP-130	273–1873 K	±6 K
A flue gas analyzer	Testo-350	0–500 ppm	±2 ppm

A comparison between the temperature measured by the experiment and the results obtained by numerical simulation is shown in Table 4. The numerical errors between them are less than 10%, and the simulation results have good reliability, so the values selected in this paper are verified. Thus, the values selected for this study can be used as simulation conditions to continue. Figure 3 shows the flame shape observed through the furnace observation window.

Table 3. Parameters for the experiments.

Parameters	Value
Velocity of air inlet (m/s)	18.92
Diameter of air inlet (m)	0.35
velocity of methane inlet (m/s)	28
Diameter of methane inlet (m)	0.141
Atmospheric temperature (K)	298
Air inlet temperature (K)	298
Excess air coefficient	1.18
Outlet pressure (Pa)	−70

Table 4. Comparison of experimental and numerical simulation results.

Thermocouple Number	Experiment	Simulation	Error
T1	1065 K	1107 K	3.9%
T2	1290 K	1349 K	4.6%
T3	1305 K	1390 K	6.5%
T4	1256 K	1295 K	3.1%

(**a**) (**b**)

Figure 3. Photographs of the rear (**a**) and front (**b**) positions of the swirler.

3. Numerical Method

Commercial CFD software was adopted for the simulations. The flow in the furnace could be regarded as a three-dimensional, stable, and uncompressible ideal flow.

3.1. Mathematic Models

The relevant physical quantities, such as combustion phenomena in the burner, must obey the laws of conservation of mass, momentum, energy, and components at a macroscopic level [24]. The expression for the mass equation is as follows:

$$\frac{\partial \rho}{\partial t} + \left[\frac{\partial \rho u}{\partial x} + \frac{\partial \rho v}{\partial y} + \frac{\partial \rho w}{\partial z}\right] = 0 \tag{3}$$

where ρ is the fluid density and u, v, and w are the velocity components of the velocity vector in the x, y, and z directions.

The expression for the momentum equation is as follows:

$$\frac{\partial(\rho u)}{\partial t} + \nabla\cdot(\rho u V) = \rho f_x + \frac{\partial \tau_{xx}}{\partial x} + \frac{\partial \tau_{yx}}{\partial y} + \frac{\partial \tau_{zx}}{\partial z} - \frac{\partial p}{\partial x} \tag{4}$$

$$\nabla\cdot(\rho v V) = \rho f_y + \frac{\partial \tau_{xy}}{\partial x} + \frac{\partial \tau_{yy}}{\partial y} + \frac{\partial \tau_{zy}}{\partial z} - \frac{\partial p}{\partial y} \tag{5}$$

$$\frac{\partial(\rho w)}{\partial t} + \nabla\cdot(\rho w V) = \rho f_z + \frac{\partial \tau_{xz}}{\partial x} + \frac{\partial \tau_{yz}}{\partial y} + \frac{\partial \tau_{zz}}{\partial z} - \frac{\partial p}{\partial z} \tag{6}$$

where τ is the viscous stress, which is divided into positive stress (e.g., τ_{xx}) and tangential stress (e.g., τ_{xy}).

The expression for the energy equation is as follows:

$$\begin{aligned}\frac{\partial}{\partial t}\left[\rho\left(e+\frac{V^2}{2}\right)\right] + \nabla\cdot\left[\rho\left(e+\frac{V^2}{2}\right)V\right] &= \rho q + \frac{\partial}{\partial x}\left(K\frac{\partial T}{\partial x}\right) + \frac{\partial}{\partial y}\left(K\frac{\partial T}{\partial y}\right) + \frac{\partial}{\partial z}\left(K\frac{\partial T}{\partial z}\right) - \frac{\partial(up)}{\partial x} \\ &- \frac{\partial(vp)}{\partial y} - \frac{\partial(wp)}{\partial z} + \frac{\partial(u\tau_{xx})}{\partial x} + \frac{\partial(u\tau_{yx})}{\partial y} + \frac{\partial(u\tau_{zx})}{\partial z} \\ &+ \frac{\partial(v\tau_{xy})}{\partial x} + \frac{\partial(v\tau_{yy})}{\partial y} + \frac{\partial(v\tau_{zy})}{\partial z} + \frac{\partial(w\tau_{xz})}{\partial x} + \frac{\partial(w\tau_{yz})}{\partial y} \\ &+ \frac{\partial(u\tau_{zz})}{\partial z} + \rho f\cdot V\end{aligned} \tag{7}$$

where e is the internal energy per unit fluid mass, q is the rate of thermal change per unit mass volume, and K is the thermal conductivity.

The expression for the component equation is as follows:

$$\frac{\partial}{\partial t}(\rho m_l) + \frac{\partial}{\partial x_j}(\rho u_j m_l + J_l) = R_l \tag{8}$$

where m_l is the l mass fraction of the component, J_l is the diffusion flux of component l, and R_l is the chemical reaction generation rate.

The main chemical reaction equations involved in the simulation are:

$$CH_4 + 1.5O_2 \rightleftharpoons CO + 2H_2O \tag{9}$$

$$CO + 0.5O_2 \rightleftharpoons CO_2 \tag{10}$$

Additionally, the main pollutant involved in the burner operation is thermal NO_x [22]. The specific chemical reaction equation is as follows:

$$O_2 \rightarrow 2O \tag{11}$$

$$O + N_2 \rightarrow N + NO \tag{12}$$

$$N + O_2 \rightarrow O + NO \tag{13}$$

$$N + OH \rightarrow H + NO \tag{14}$$

The realizable k-ε turbulence model is used as the turbulent model [25]. Its governing equation is given by

$$\frac{\partial}{\partial t}(\rho k) + \frac{\partial}{\partial x_j}(\rho k u_j) = \frac{\partial}{\partial x_j}\left[\left(\mu + \frac{\mu_t}{\sigma_k}\right)\frac{\partial k}{\partial x_j}\right] + G_k + G_b - \rho\varepsilon - Y_M + S_K \tag{15}$$

$$\frac{\partial}{\partial t}(\rho\varepsilon) + \frac{\partial}{\partial x_i}(\rho\varepsilon u_j) = \left[\frac{\partial}{\partial x_j}\left(\mu + \frac{\mu_t}{\sigma_\varepsilon}\right)\frac{\partial \varepsilon}{\partial x_j}\right] + \rho C_1 S\varepsilon - \rho C_2\frac{\varepsilon^2}{k+\sqrt{\nu\varepsilon}} + C_{1\varepsilon}\frac{\varepsilon}{k}C_{3\varepsilon}G_b + S_\varepsilon \tag{16}$$

where $C_1 = \max\left[0.43, \frac{\eta}{\eta+5}\right]$, $\eta = S\frac{k}{\varepsilon}$, $S = \sqrt{2S_{ij}S_{ij}}$. where G_k represents the generation of turbulence kinetic energy due to the mean velocity gradient. G_b is the generation of turbulence kinetic energy due to buoyancy. Y_M represents the contribution of the fluctuation in compressible turbulence to the overall dissipation rate. C_2 and $C_{1\varepsilon}$ are constant. σ_k and σ_ε are the turbulent Prandtl numbers for k and ε, respectively. S_K and S_ε are user-defined source terms.

The physics of the interaction between turbulent and chemical reactions is described by the eddy dissipation model, where detailed Arrhenius chemical kinetics can be put into the turbulent reacting flow. At the same time, radiation must be taken into account to acquire realistic results of temperature, so the discrete ordinates radiation model (DO) is used to calculate heat transfer. External emissivity and internal emissivity are equal to 1 and 0.6, respectively. Besides, gravity is also considered. The semi-implicit method for pressure-linked equations (SIMPLE) is used for velocity-pressure coupling. The items of turbulent kinetic energy, turbulent dissipation rate, species, etc. are applied first order upwind for spatial discretization, and it is changed to second order upwind to improve the calculation precision after the calculation converged. The residual criteria for energy and radiation intensity are set to 10^{-6}, while for other governing equations, to 10^{-4}.

3.2. Grid Independence

The quality of the grid has an influence on the accuracy of the calculation. Due to the irregular shape of the combustion chamber, unstructured tetrahedral grids are used. In this study, three different grid sizes are selected for independent study of the same burner model. The axial velocity on the central axis of the burner is chosen as an indicator to test the sensitivity of the results to the different grid sizes and the results are shown in Figure 4. The results for the coarse grid differ from the other two types. In contrast, the profiles of the medium and fine grids have similar trends and mainly overlap at each point. As a result, a medium grid number of 8.5 million is used for this study.

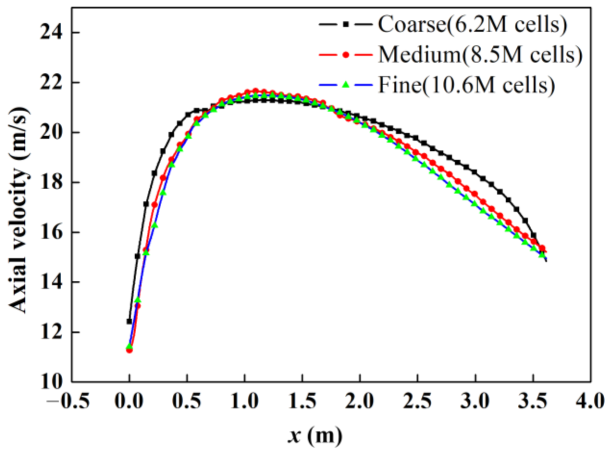

Figure 4. Axial velocity profiles for different grids.

4. Results and Discussions

It is appropriate to change the geometrical parameter and flow parameter to achieve low-emission NO. These combustors are named general combustors (GC). On the basis of the general combustor, we vary the equivalence ratio of the tertiary air area by changing the number and diameter of the nozzles on the circumference of the inner and outer supply rings, and the combustor is named as a new combustor (NC). Specific parameters are shown in Table 5.

Table 5. Parameters for GC and NC.

Name	Angle of PASV [1]	Angle of SASV [2]	Swirl Number (S)	Nozzle Number on O/ICTOGSR [3]	Nozzle Diameter (mm)	Nozzle Number on O/ICTIGSR [4]	Nozzle Diameter (mm)
GC30	58	30	0.47	30/56	5.25/4, 3.5	28/28	3/3.5
GC44	58	44	0.78	30/56	5.25/4, 3.5	28/28	3/3.5
GC58	58	58	1.29	30/56	5.25/4, 3.5	28/28	3/3.5
NC58	58	58	1.29	60/28	4.5/4	28/28	3/3.5

[1] PASV: primary-air swirl vane; [2] SASV: secondary-air swirl vane; [3] O/ICTOGSR: the outer/inner circumference of the outer gas supply ring; [4] O/ICTIGSR: the outer/inner circumference of the inner gas supply ring.

4.1. Effect of Swirl Number of Outer Swirling Flow on Combustion

In this paper, the total air mass flow rate and total fuel are fixed, i.e., the load condition is the same. The influence of back pressure on airflow distribution behind the draft fan is obvious from Figure 5, which affects the air flow rate through the primary stage (the annular swirler). There are possible solutions to improve this phenomenon. The first option is to increase the distance between the draft fan and the swirler.

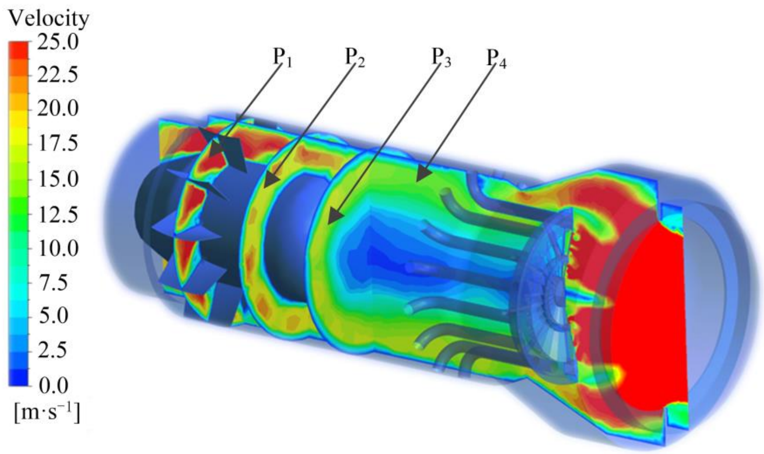

Figure 5. The velocity contours of different section. (P_1: $x = -3.8$ m; P_2: $x = -3.5$ m; P_3: $x = -3.2$ m; P_4: $z = 0$).

In the non-reaction case, the area-weighted average of methane mass fraction obtained at different sections within the range from the swirler to combustor exit. Methane mass fraction is the percentage of methane mass in the total mass. As shown in Figure 6, the methane distribution is more uniform as the swirl number increases, because the larger turbulence intensity caused by the high swirl number of the outer swirler provides the energy for mass transfer between air and methane, resulting in the strongest mixing with a large expansion angle of the airflow. In addition, there is a sudden change at $x = -100$ mm, which is caused by the reduced area. It can also be seen from Figure 5 that the values are not much different close to the swirler, and the reason for this is that mass transfer requires a certain amount of distance after the methane is sprayed.

At this point, it can also be seen that turbulent mixing consumes a large amount of kinetic energy with swirl number equal to 1.29, as shown in Figure 7, so the axial velocity decay is accelerated. Moreover, no central recirculation zone is formed for GC40 and GC30. The air flow rate passing through the swirler is relatively small and rotation intensity is weak, so the flow field formed by the vortex breaking downstream of the swirler is not completely diffused and is scattered by the peripheral high-speed jet, resulting in instability of the vortex structure. Yet, the formation of small-scale recirculation zones on both sides near the swirler maintains the stability of the flame.

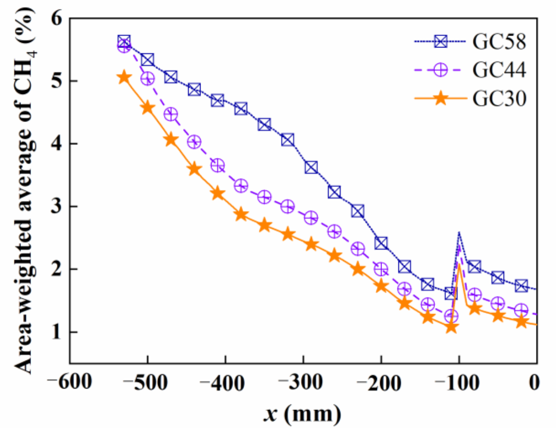

Figure 6. The area-weighted average of methane mass fraction at different section within hood.

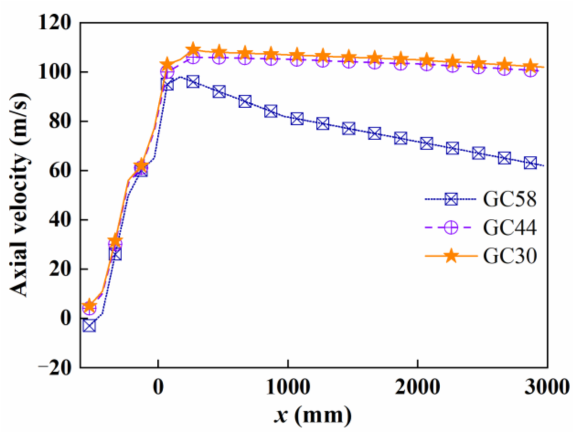

Figure 7. The axial velocity along central axis.

The tangential velocity is small for the GC44 and GC30, resulting in the mixing process of methane and air being longer, so the high temperature range of the two combustors is wider. However, there are obviously differences between them and GC58. As shown in Figure 8, the temperature of GC58 is the lowest in the entire region. The reason for this may be that the methane and air are uniformly mixed.

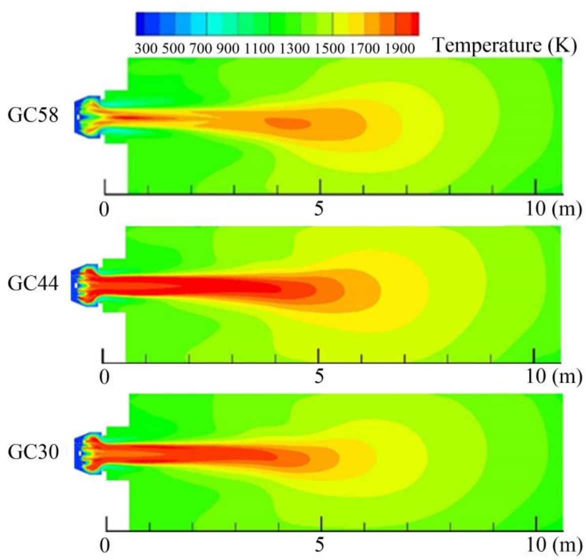

Figure 8. The distribution of Temperature for GC58, GC44 and GC30 at $z = 0$.

Compared to the O_2 distribution shown in Figure 9, the range of oxygen concentration is the largest for GC58. The lowest air flow rate was obtained for air passing through the swirler for GC58, and this means that more oxygen is carried by the peripheral jet downstream. Compared to the CO distribution shown in Figure 10, CO is an intermediate product during the combustion of methane, and it is a reducing gas. This variable is important to reduce the amount of nitrogen oxides produced. The N_2 in the air generates NO in a high temperature and oxygen-rich environment, but the NO is reduced under a reducing atmosphere of CO. During the combustion process using natural gas as fuel, the nitrogen oxides produced are mainly thermal NO.

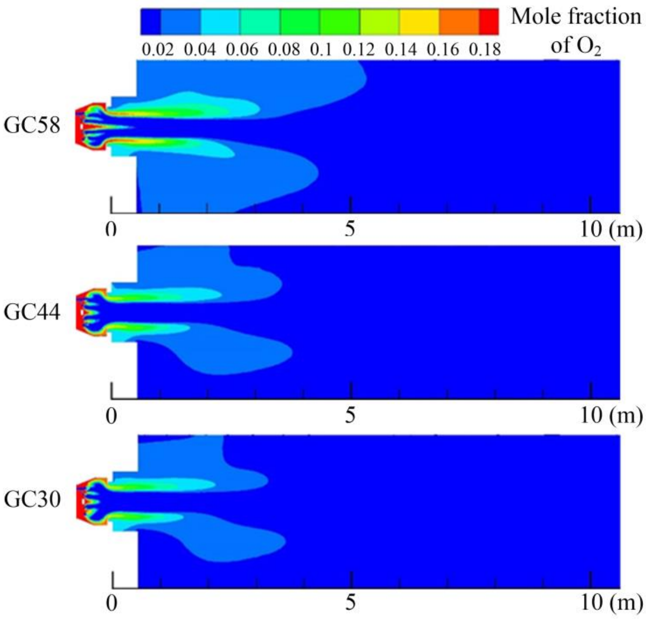

Figure 9. The distribution of Mole fraction of O_2 for GC58, GC44 and GC30 at z = 0.

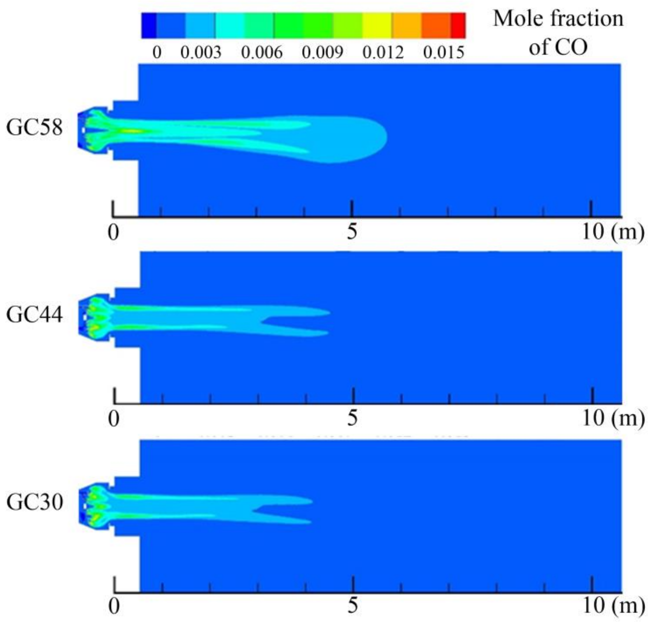

Figure 10. The distribution of Mole fraction of CO for GC58, GC44 and GC30 at z = 0.

It is worth noting that the statistical plane is a circular plane with a radius equal to 0.625 m within the furnace shown in Figure 11. Because the operating parameters and combustor positions are the same, the trends of each variable are similar. So, we can draw some conclusions.

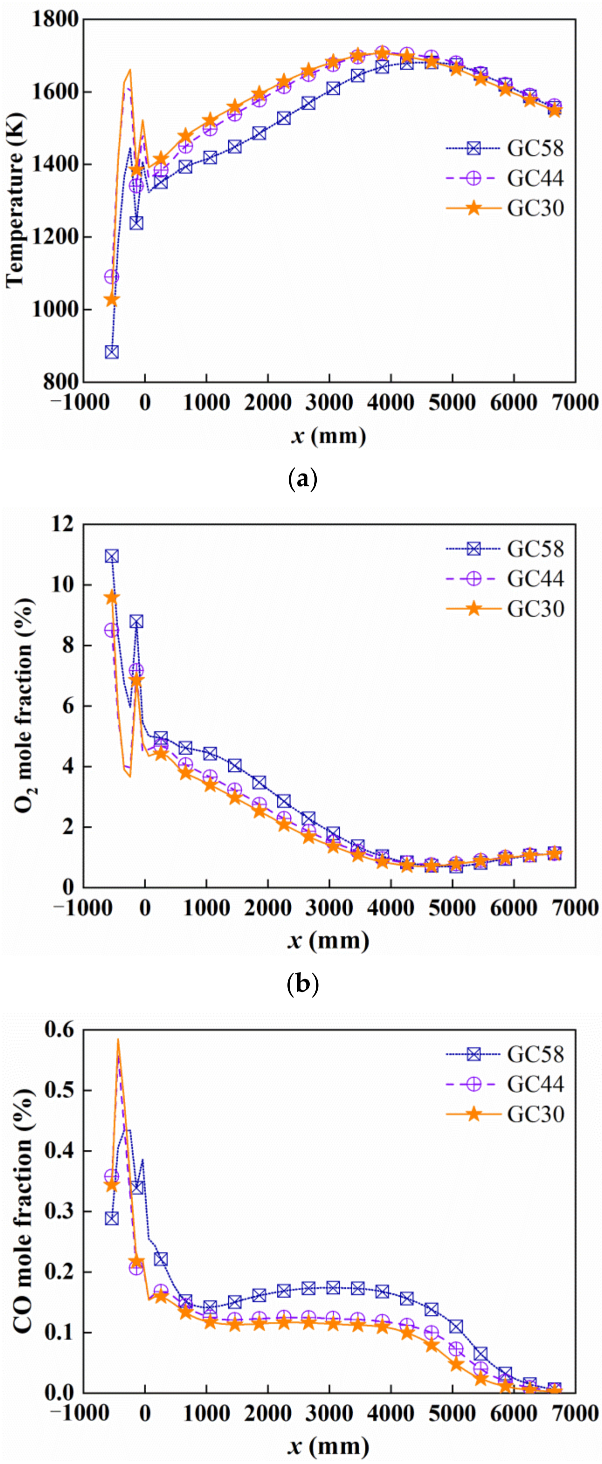

(**a**)

(**b**)

(**c**)

Figure 11. Distribution of the average temperature and species mole fraction along *x*-axis. (**a**) Temperature distribution. (**b**) O_2 mole fraction distribution. (**c**) CO mole fraction distribution.

We can see that the temperature of GC58 is lower than the other two combustors shown in Figure 11a. Despite the air being more strongly mixed with methane, the amount of air flowing through the outer swirler is the smallest, so the amount of heat released is low in the case of insufficient air. However, the temperature profiles basically coincide with the other two combustors. The air flow rate through the outer swirler is essentially uniform for GC44 and GC30, so the trend of temperature is similar. The mole fraction of O_2 has dropped sharply near the swirler shown in Figure 11b. This means that a large amount of heat is released near the swirler. This causes a dramatic increase in temperature, as shown in Figure 10. The mole fraction of O_2 suddenly rises at a certain position. The reason for this is that this position is near the constricted section of the hood, which corresponds to the temperature profile. Besides, the O_2 consumption rate of GC58 is significantly higher than others in the furnace, and this is consistent with the previous conclusion. The peaks of GC40 and GC30 are 50% higher than GC58, as shown in Figure 11c. Because the air flow rate through the outer swirler is greater than GC58, a large amount of CO is formed according to the chemical reaction mechanism.

NO gradually decreases as the blade angle of the outer swirler increases, as shown in Figure 12. The difference between GC58 and the other two is greater because of the lower temperature in the furnace. Furthermore, the experiment showed the same pattern.

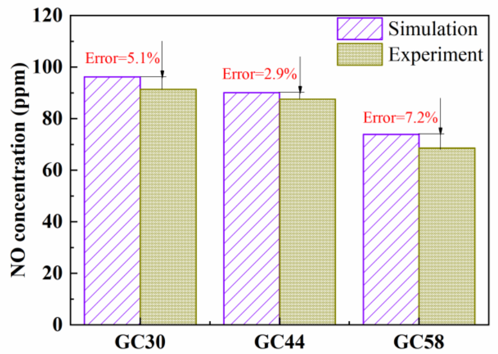

Figure 12. NO concentration at the furnace outlet.

4.2. The Effect of Equivalent Ratio on Combustion

In addition to the uniformity of mixing, the equivalence ratio of mixed gas at each level also affects NO emissions. Due to the influence of the draft fan on the airflow, the effect of gas placement on each swirler is explored by improving the GC58. It can be seen from Figure 13a that NC58 has a wide range of high temperature zones. GC58 has a relatively narrow high temperature zone. The O_2 distribution range in NC58 is narrower than that of GC58 from Figure 13b. In other words, a large amount of O_2 is being consumed upstream. It can be seen from Figure 13c, whether in the hood or upstream of the furnace, the mole fraction of CO is higher and the distribution range is larger in the same region.

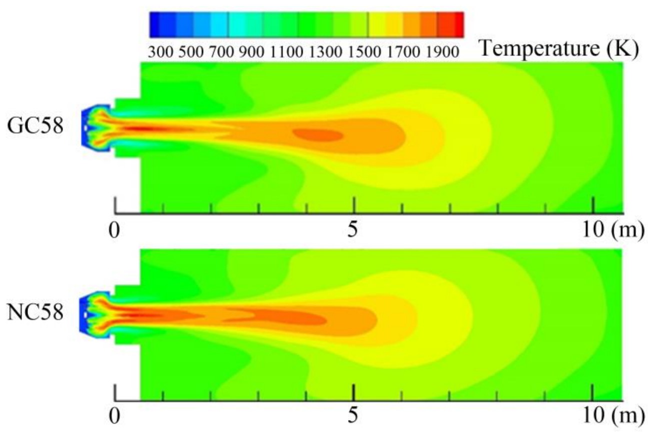

(**a**) Temperature distribution

Figure 13. *Cont.*

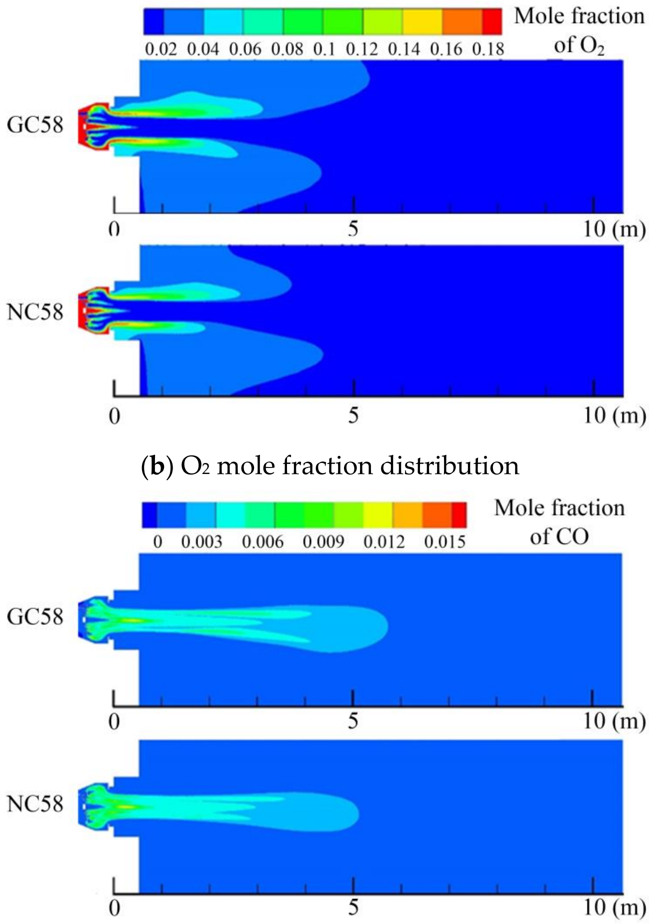

(**b**) O_2 mole fraction distribution

(**c**) CO mole fraction distribution

Figure 13. The distribution of (**a**) Temperature (**b**) Mole fraction of O_2 and (**c**) CO for NC58 compared to GC58 at $z = 0$.

The air flow rate at each swirler is the same since the geometry does not change. The temperature gradually rises and reaches a peak, and is about 100 K higher than GC58 during $x = 0$ to $x = 4.5$ m as shown in Figure 14a. The reason for this is that more methane is ejected through the OCTOGSR (outer circumference of the outer gas supply ring) and the local equivalence ratio is improved. However, the temperature continues to rise for GC58 from $x = 4.5$ to $x = 5.3$ m, so it can be inferred that there is still a small amount of methane that is not completely burning, and the mixing effect is not satisfactory. Additionally, the flame length of NC58 is shorter than that of GC58, and more adaptable to industrial furnaces.

The O_2 mole fraction shown in Figure 14b is substantially similar within the hood. The value is lower than GC58 from $x = 0$ to $x = 4.5$ m, which indicates that the mixing effect is better than GC58. Besides, this is consistent with the temperature profile. The CO mole fraction of NC58 is higher than GC58 because of adequate methane and air reacting at $x < 1.75$ m, shown Figure 14c, producing more CO.

From the combination of Figures 15 and 16, it can be concluded that increasing the equivalent ratio of the tertiary air region improves the mixing efficiency of gas and air, which reduces the NO at the furnace outlet. Thus, the combustion performance of NC58 is better than GC58.

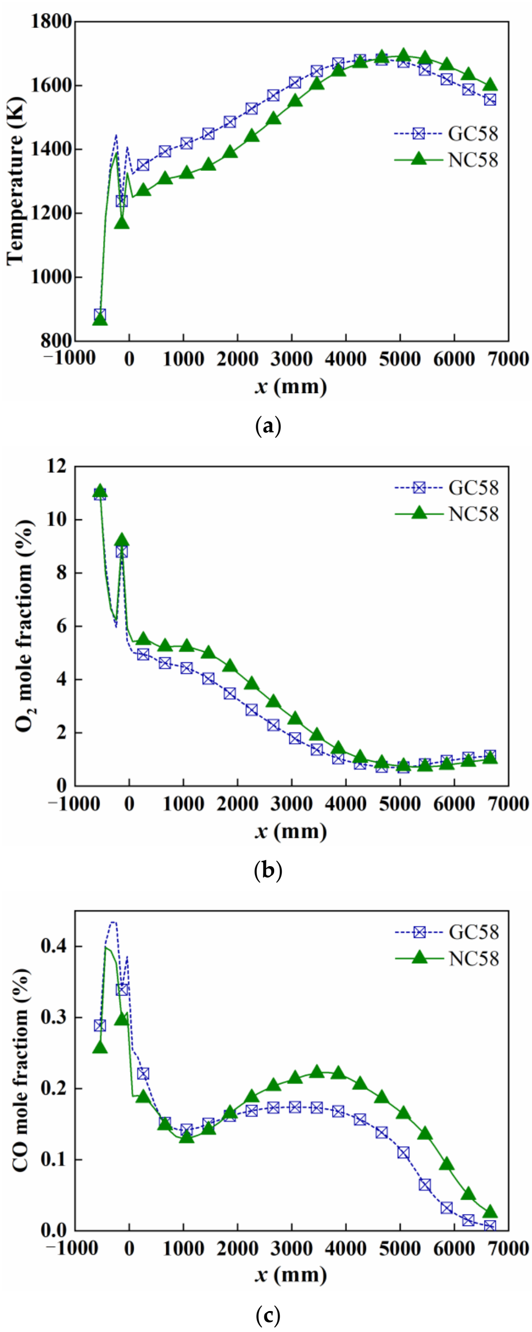

Figure 14. Distribution of the average temperature and species mole fraction along *x*-axis. (**a**) Temperature distribution. (**b**) O_2 mole fraction distribution. (**c**) CO mole fraction distribution.

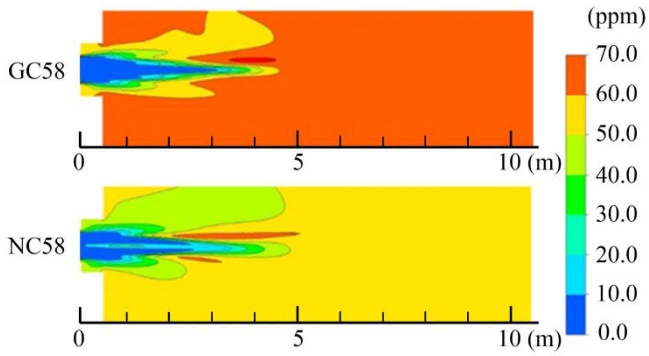

Figure 15. The distribution of NO for GC58 and NC58.

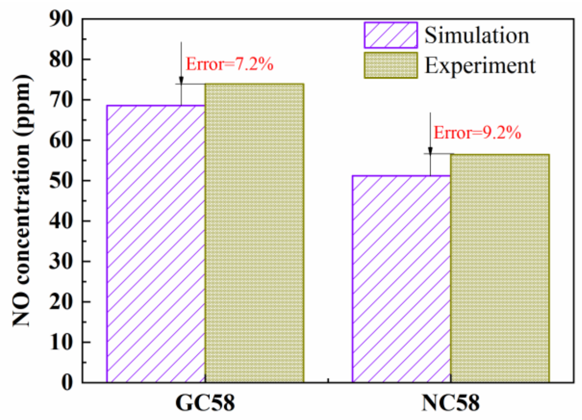

Figure 16. NO concentration at the furnace outlet.

5. Conclusions

Experimental and numerical studies were performed on a non-premixed, full-scale industrial combustor used at an asphalt mixing station. The correctness of the selected numerical model is verified by experiments. The results of this study could provide an important theoretical basis for the design of non-premixed burners. Salient outcomes of the present research are:

(a) The presence of the backpressure behind the draft fan affects the distribution of the air flow rate, so the air flowing through the swirler accounts for a small proportion of the total air volume. Moreover, the air flow rate through each swirler changes as the angle of the outer swirler changes.

(b) The rotating ability of the airflow is weak for GC40 and GC30, which causes the vortex to be dissipated by the high-speed tertiary air, so there is no central recirculation zone. As the angle of the outer swirler blades increases, the combustion is more evenly distributed, which indicates better combustion characteristics. As a result, the NO emissions are gradually reduced as the angle of the outer swirler blades increases. Non-premixed burners can be designed to increase the angle of the external swirler, which will reduce NO emissions. Besides, the joint effect of the blade angles of the annular swirler and the outer swirler will be further studied in future work.

(c) When the air flow rate at each level is basically the same, increasing the equivalence ratio of the tertiary air area will significantly reduce NO emissions. It is also indicated that the average temperature is 100 K higher than a general combustor with 58° blade angle in the furnace by increasing the equivalent ratio of the tertiary air area, and the NO emissions reduced by approximately 25%. This provides a good basis for the subsequent development and improvement of the combustor.

Author Contributions: Conceptualization, J.L. and M.B.; methodology, M.B.; software, M.B.; validation, J.L., F.Z., Y.Z. and J.Y.; formal analysis, J.L.; investigation, F.Z.; resources, J.Y.; data curation, J.L. and M.B.; writing—original draft preparation, J.L. and M.B.; writing—review and editing, M.B.; visualization, M.B.; supervision, J.L.; project administration, J.L.; funding acquisition, J.L. All authors have read and agreed to the published version of the manuscript.

Funding: This work is supported by the National Natural Science Foundation of China (52075188), Pilot Project of Fujian Province (2018H0021), Project of Quanzhou Science and Technology (2021G05).

Institutional Review Board Statement: Not applicable.

Informed Consent Statement: Not applicable.

Data Availability Statement: Not applicable.

Conflicts of Interest: The authors declare no conflict of interest.

References

1. Li, X. Design of energy-conservation and emission-reduction plans of China's industry: Evidence from three typical industries. *Energy* **2020**, *209*, 118358. [CrossRef]
2. Zhou, L.X. Comparison of studies on flow and flame structures in different swirl combustors. *Aerosp. Sci. Technol.* **2018**, *80*, 29–37. [CrossRef]
3. Mansouri, Z.; Boushaki, T. Experimental and numerical investigation of turbulent isothermal and reacting flows in a non-premixed swirl burner. *Int. J. Heat Fluid Flow* **2018**, *72*, 200–213. [CrossRef]
4. Zhang, J.; Sun, Y.; Li, J.; He, X. Study on the Hybrid Cooling of the Flame Tube in a Small Triple-Swirler Combustor. *Energies* **2020**, *13*, 5554. [CrossRef]
5. Yuan, Y.; Zeng, Q.; Yao, J.; Zhang, Y.; Zhao, M.; Zhao, L. Improving Blowout Performance of the Conical Swirler Combustor by Employing Two Parts of Fuel at Low Operating Condition. *Energies* **2021**, *14*, 1681. [CrossRef]
6. Vigueras-Zúñiga, M.O.; Ramírez-Ruíz, C.A.; Herrera-May, A.L.; Tejeda-del-Cueto, M.E. Numerical and Experimental Analysis of the Effect of a Swirler with a High Swirl Number in a Biogas Combustor. *Energies* **2021**, *14*, 2786. [CrossRef]
7. Li, S.; Chen, Z.; Li, X.; Jiang, B.; Li, Z. Effect of outer secondary-air vane angle on the flow and combustion characteristics and NO_x formation of the swirl burner in a 300-MW low-volatile coal-fired boiler with deep air staging. *J. Energy Inst.* **2017**, *90*, 239–256. [CrossRef]
8. Li, G.; Jiang, X.; Zhu, J.; Yang, J.; Liu, C.; Mu, Y.; Xu, G. Combustion control using a lobed swirl injector and a plasma swirler. *Appl. Therm. Eng.* **2019**, *152*, 92–102. [CrossRef]
9. Banu, J.P.; Mani, A. Numerical studies on ejector with swirl generator. *Int. J. Therm. Sci.* **2019**, *137*, 589–600. [CrossRef]
10. Zhang, R.; Xu, Q.; Fan, W. Effect of swirl field on the fuel concentration distribution and combustion characteristics in gas turbine combustor with cavity. *Energy* **2018**, *162*, 83–98. [CrossRef]
11. Boushaki, T.; Merlo, N.; Chauveau, C.; GöKalp, I. Study of pollutant emissions and dynamics of non-premixed turbulent oxygen enriched flames from a swirl burner. *Proc. Combust. Inst.* **2016**, *36*, 3959–3968. [CrossRef]
12. Zhou, H.; Yang, Y.; Liu, H.; Hang, Q. Numerical simulation of the combustion characteristics of a low NO_x swirl burner: Influence of the primary air pipe. *Fuel* **2014**, *130*, 168–176. [CrossRef]
13. Johnson, M.R.; Littlejohn, D.; Nazeer, W.A.; Smith, K.O.; Cheng, R.K. A comparison of the flowfields and emissions of high-swirl injectors and low-swirl injectors for lean premixed gas turbines. *Proc. Combust. Inst.* **2005**, *30*, 2867–2874. [CrossRef]
14. Cozzi, F.; Coghe, A. Effect of air staging on a coaxial swirled natural gas flame. *Exp. Therm. Fluid Sci.* **2012**, *43*, 32–39. [CrossRef]
15. Almeida, D.; Lacava, P.T. Analysis of Pollutant Emissions in Double-stage Swirl Chamber for Gas Turbine Application. *Energy Procedia* **2015**, *66*, 117–120. [CrossRef]
16. Sung, Y.; Choi, G. Effectiveness between swirl intensity and air staging on NO_x emissions and burnout characteristics in a pulverized coal fired furnace. *Fuel Process. Technol.* **2015**, *139*, 15–24. [CrossRef]
17. Zeng, Q.; Dong, Z.; Yuan, Y. Counter-rotating dual-stage swirling combustion characteristics of hydrogen and carbon monoxide at constant fuel flow rate. *Int. J. Hydrogen Energy* **2020**, *45*, 4979–4990. [CrossRef]
18. Elbaz, A.M.; Moneib, H.A.; Shebil, K.M.; Roberts, W.L. Low NO_X-LPG staged combustion double swirl flames. *Renew. Energy* **2019**, *138*, 303–315. [CrossRef]
19. Mazaheri, K.; Shakeri, A. Numerical optimization of laboratory combustor geometry for NO suppression. *Appl. Therm. Eng.* **2016**, *102*, 1328–1336. [CrossRef]
20. Khatir, Z.; Thompson, H.; Kapur, N.; Toropov, V.; Paton, J. Multi-objective Computational Fluid Dynamics (CFD) design optimisation in commercial bread-baking. *Appl. Therm. Eng.* **2013**, *60*, 480–486. [CrossRef]
21. Mansouri, Z.; Aouissi, M.; Boushaki, T. Numerical computations of premixed propane flame in a swirl-stabilized burner: Effects of hydrogen enrichment, swirl number and equivalence ratio on flame characteristics. *Int. J. Hydrogen Energy* **2016**, *41*, 9664–9678. [CrossRef]
22. Fu, Z.; Gao, H.; Zeng, Z.; Liu, J.; Zhu, Q. Generation characteristics of thermal NO_x in a double-swirler annular combustor under various inlet conditions. *Energy* **2020**, *200*, 117487. [CrossRef]
23. Marosky, A.; Seidel, V.; Sattelmayer, T.; Magni, F.; Geng, W. Impact of Cooling Air Injection on the Combustion Stability of a Premixed Swirl Burner Near Lean Blowout. *J. Eng. Gas Turb. Power* **2013**, *135*, 111501. [CrossRef]
24. Tang, Y.; Liu, Z.; Li, Y.; Zhao, F.; Chua, K.J. Mixing process of two streams within a steam ejector from the perspectives of mass, momentum and energy transfer. *Appl. Therm. Eng.* **2020**, *185*, 116358. [CrossRef]
25. Yáez-Varela, J.; González-Neria, I.; Alonzo-García, A.; Rivadeneyra-Romero, G.; Martínez-Delgadillo, S. Numerical analysis of the hydrodynamics induced by rotating ring electrode using κ-ε models. *Chem. Eng. Process.* **2020**, *158*, 108203. [CrossRef]